JMEPEG (2024) 33:5487–5500
https://doi.org/10.1007/s11665-024-09417-3

1059-9495/$19.00

ORIGINAL RESEARCH ARTICLE

Correlation Between Pressureless Sintering, Microstructure, and Properties of ZrB_2-SiC-Y_2O_3 Composites

S. Sarkar, M.K. Mondal, and M. Mallik

Submitted: 15 March 2023 / Revised: 7 March 2024 / Accepted: 12 March 2024 / Published online: 8 April 2024

The influence of Y_2O_3 addition on densification, physical, mechanical, thermal, and oxidation properties of ZrB_2-20 vol.%SiC- (0-15 vol.%Y_2O_3) composites was investigated in the present study. Powders of ZrB_2-SiC-Y_2O_3 were cold compacted uniaxially, and green compacts were densified by pressure-less sintering. Results indicate that Y_2O_3 addition improves the sinterability and mechanical properties, whereas it diminishes the electrical and thermal conductivities of the investigated composites. Removal of surface oxides by the additives and segregation of Y_2O_3 particles at the triple junction of the ZrB_2 grains enhances densification. Reduction in porosity (9.5-4.2%) through Y_2O_3 addition (0-15 vol.%) improves hardness (up to 52%), relative elastic modulus (up to 9%), and fracture toughness (up to 26%) of the investigated composites. The electrical conductivity has been observed to vary in the range of 2.67-1.92 10^6 S/m, and thermal diffusivity values decrease with an increase in Y_2O_3 content and temperature. Oxidation studies indicate that the ZrB_2-SiC composite shows better oxidation resistance than other investigated composites. Characterization of oxidized scales confirms the formation of a thicker oxide layer over the samples containing Y_2O_3.

Keywords oxidation, pressure-less sintering, ultra-high temperature ceramics, zirconium diboride

1. Introduction

Ceramics exhibiting excellent metallurgical stability above 2000 °C, with higher melting temperature (> 3000 °C), are considered Ultra High-Temperature Ceramics (UHTCs). In an oxidizing environment, these ceramics form a protective superficial Oxide layer. This oxide layer must be dense, continuous, stable, and particularly adhesive to the surface during thermal cycles involved in many applications. Generally, borides, nitrides, and carbides of transition metals are known as UHTCs. Among these, zirconium diboride (ZrB_2) has the lowest theoretical density (6.09 g/cm^3) in the diboride group (Ref 1-5).

UHTCs have found applications in hypersonic space vehicles, rocket propulsion, sharp surfaces of re-entry vehicles, components for furnaces, etc. Moreover, the application should last many years (Ref 6-9). So, studying material long-term oxidation behavior for a long exposure time is required. Though Zirconium and hafnium diborides are popular as UHTCs, they possess meager oxidation resistance. A passive film of liquid B_2O_3 is formed over the parent material. Thus, it fills pores, protecting the unoxidized material from further oxidation. When the temperature rises above 1200 °C, the liquid B_2O_3 film evaporates, and a perforated layer of ZrO_2 is formed; thus, the parent material starts to oxidize continuously (Ref 10-13).

Many researchers have focused on improving ultra-high-temperature ceramics to overcome this limitation. Three main drawbacks are evident in ZrB_2-based ceramics: comparatively poor fracture toughness, lower sinterability because Zr forms strong bonding with B covalently, and becomes less oxidation resistant at high temperatures. Different researchers have taken several measures to overcome these limitations of ZrB_2-based ceramics. $MoSi_2$, SiC, or carbon fibers were induced to improve mechanical properties. However, reinforcement over a range reduces the sinterability of ZrB_2. For the improvement of the sintered density of ZrB_2 few steps are taken-sinter operation done at high temperatures (> 2000 °C), pressure-assisted sintering, and using sintering additives (Ref 14-20).

In recent times ZrB_2 based ceramic matrix composites has been the focus of many researchers for high-temperature use as it is aggregated of higher melting point (Ref 5), good chemical inactivity, excellent thermal shock resistance (Ref 21, 22),

This article is an invited submission to the *Journal of Materials Engineering and Performance* selected from presentations at the 4th International Conference on Processing & Characterization of Materials (ICPCM 2022) held December 9–11, 2022, at the National Institute of Technology, Rourkela, Odisha, India. It has been expanded from the original presentation. The issue was organized by Prof. Joao Pedro Oliveira, Universidade NOVA de Lisboa, Portugal; Prof. B. Venkata Manoj Kumar, Indian Institute of Technology Roorkee, India; Dr. D. Arvindha Babu, DMRL, DRDO, Hyderabad, India; Prof. Kumud Kant Mehta and Prof. Anshuman Patra, National Institute of Technology Rourkela, Odisha, India; and Prof. Manab Mallik, National Institute of Technology Durgapur, India.

S. Sarkar, M.K. Mondal, and **M. Mallik**, Department of Metallurgical and Materials Engineering, National Institute of Technology Durgapur, Durgapur, India. Contact e-mail: manab.mallik@mme.nitdgp.ac.in.

higher electrical and thermal conductivity (Ref 23-26), good wear resistance (Ref 27-29) better mechanical properties (Ref 30-38) and good creep resistance (Ref 39). Many researchers reported that SiC addition improves the oxidation resistance of ZrB_2 by forming a borosilicate layer that protects at higher temperatures, but pure SiO_2 melts at 1726 °C (Ref 40).

Besides improving oxidation behavior (Ref 41-43), SiC enhances the strength and toughness of ZrB_2 ceramics. Chamberlain et al. (Ref 44) reported that introducing 20 or 30 vol.% SiC particles increases the strength of the ZrB_2 composite from ~560 to 1000 MPa. As per the work of Monteverde, the addition of 10 vol.% of fine SiC particle improves the fracture strength of hot-pressed ZrB_2 350 to 835 MPa (Ref 45). Due to lower self-diffusion coefficients and strong covalency between ZrB_2 & SiC, this binary composite can fabricate with high density by hot pressing or reaction hot-pressing. Generally simpler shapes like disk-shaped samples are made by hot-pressing, and after that, they are taken for machining for required shapes. The latest research has proved that almost the theoretical density of ZrB_2–SiC can be attained by pressureless sintering (PS), removing the primary limitations of this ceramics (Ref 15-20, 26, 35, 46).

The flexure strength of the ZrB_2–SiC composite was recorded as less than 400 MPa by adding SiC grains of an average size of ~6 μm. When SiC particles having an average size of ≤ 1 μm were used, flexure strength increased to 900 MPa (Ref 47).

Above 2000 °C, the protective borosilicate layer gets degraded, so the internal parent material continuously oxidizes by active oxidation. Han et al. (Ref 48) reported that at 2200 °C in an oxy-acetylene torch experiment, the residual perforated ZrO_2 layer might form a thick protective ZrO_2 layer by sintering. Diffusivity of oxygen through the thick ZrO_2 layer is higher than that of SiO_2 layer.

Furthermore, several researchers studied oxidation kinetics related to mass change analysis, supporting that the borosilicate layer protects from further oxidation do not particularly correspond to the formation of oxide scale due to the vaporization of B_2O_3 and CO_2. In the work of Zhang et al. (Ref 49), mass change kinetics was reported, and the calculated oxidation exponent for monolithic ZrB_2 and ZrB_2-4wt.%WC were 1 and ~2, respectively.

Adding 3 vol.% of Y_2O_3 reduces the impurity present on the surface of starting powder by reaction with these oxides viz. ZrO_2, B_2O_3 and SiO_2. This phenomenon helps increase the density of ZrB_2-SiC as removing impurity oxides impressively reduces the excessive grain growth. Flexural strength and fracture toughness also increased as the sinterability and microstructure get enhanced. Comparatively higher amount addition of Y_2O_3, i.e., 8 vol.%, exhibits insufficient enhancement in the mechanical properties probably because the excess additive creates the unwanted liquid phase at grain boundaries (Ref 50).

Zhi-Qiang Cheng et al. (Ref 51) studied pressure-less sintered ZrB_2-SiC ceramics. Y_2O_3 and Al_2O_3 were added for better densification. The study shows how the sintering additives and crystallization annealing at 1350 °C affect the structure and properties of the composite. Therefore, the current study focuses on the influence of Y_2O_3 content on the densification, microstructure, physical and mechanical properties, and oxidation performance of ZrB_2-20 vol.%SiC composites.

2. Experimental Techniques

In this pressure-less sintering of Zirconium diboride based composites used, raw powders of highly pure zirconium diboride (ZrB_2), silicon carbide (SiC), boron carbide (B_4C), graphite and yttrium oxide (Y_2O_3) powders as raw materials. Powder compositions of ZSBC-0Y (ZrB_2-20 vol.% SiC 5.5 vol.% B_4C 3 vol.% Graphite powder), ZSBC-5Y (ZrB_2-20 vol.% SiC 5.5 vol.% B_4C 3 vol.% Graphite powder 5 vol.% Y_2O_3), ZSBC-10Y (ZrB_2-20 vol.% SiC 5.5 vol.% B_4C 3 vol.% Graphite powder 10 vol.% Y_2O_3) and ZSBC-15Y (ZrB_2-20 vol.% SiC 5.5 vol.% B_4C 3 vol.% Graphite powder 15 vol.% Y_2O_3) were prepared by mixing. The sintering additives used were graphite and B_4C powders. The mixed composite powders were uniaxially compacted by a pressure of 333 MPa. Densification of the green compacts was densified by pressure-less sintering at 1750 °C for 30 minutes in an argon atmosphere. The effect of Y_2O_3 content on Bulk density, densification parameter, and shrinkage were calculated using Eqs 1 and 2, respectively.

$$\psi = \frac{\rho_s - \rho_G}{\rho_T - \rho_G} \quad \text{(Eq 1)}$$

$$\rho_s = \frac{\rho_G}{\left(1 - \frac{\Delta L}{L_0}\right)} \quad \text{(Eq 2)}$$

where ψ, ρ_s, ρ_G, ρ_T and $\Delta L/L_0$ are densification parameter, sintered density, green density, theoretical density, and shrinkage, respectively.

Archimedes' principle was used to compute the density of the composites. Phase analysis of the sintered composites was studied by x-ray Diffraction analysis. Field emission scanning electron microscopy (FESEM) assisted with an energy dispersive x-ray (EDX) attachment was utilized to investigate the microstructures of the pressureless sintered pellets.

To study the electrical resistivities of the sintered composites at ambient temperature with the help of a high precision resistivity unit functioning on the four-wire probe mechanism was used. Samples were machined from the sintered composites to measure the electrical resistivity according to Eq 3:

$$r_s = \frac{\pi t R}{\ln 2} \quad \text{(Eq 3)}$$

where r_s is electrical resistivity, R is resistance of the sample, and t denote the thickness of the composite. Electrical conductivity (σ) was estimated as:

$$\sigma = \frac{1}{r_s} \quad \text{(Eq 4)}$$

The thermal diffusivity of the developed composites was studied utilizing the laser flash method following the ASTM E−1461 standard (Ref 52). The measuring principle includes a high-intensity laser energy pulse directed on disc-shaped samples (diameter and thickness were 12.5 and 1.5 mm, respectively) for a short duration. The incident energy that is absorbed by the bottom surface of the samples causes an enhancement in the temperature of the top face, which is recorded with time. The duration at which the absorbed energy reaches 50% of the maximum value is termed half-time ($t_{1/2}$). The thermal diffusivity (α) is computed from the relation (Ref 5):

$$\alpha = \frac{0.13879L^2}{t_{1/2}} \quad \text{(Eq 5)}$$

where (L) is the thickness of the specimen. Specific heat (c) of the composites were evaluated from earlier reported data (Ref 53) for each constituent phase. Subsequently, the thermal conductivity (λ) was measured by the relation 6:

$$\lambda = c\alpha\rho \quad \text{(Eq 6)}$$

where ρ is the density of the composite at 20 °C.

Elastic modulus (E) of the composites were calculated utilizing the following relation:

$$E = E_0\left(1 - 1.9P + 0.9P^2\right) \quad \text{(Eq 7)}$$

Here, E_0 is the elastic modulus of the sample devoid of any porosity, and P is the volume fraction of the porosity present in the composites. E_0 has been calculated exercising rule of mixture (ROM) and using elastic modulus of ZrB_2 = 500 GPa, SiC = 475 GPa, and Y_2O_3 = 171.5 GPa. Vickers microhardness tests were carried out at a load of 500gf for 15 seconds to determine the hardness of the composites whereas, at the load of 2 kgf for 15 s, was employed for studying the indentation fracture toughness (IFT), K_{IC}. The model proposed by Anstis et al. (Ref 54) has been utilized to calculate the IFT of the investigated composites.

$$K_{IC} = 0.016\left(\frac{E}{H}\right)^{1/2}\frac{P}{C^{3/2}} \quad \text{(Eq 8)}$$

where E = Young's modulus, H = hardness, P = load. Furthermore, a and l are the half diagonal length of indentation and the crack length, respectively (wherein $c = l + a$). The crack lengths and the lengths of indentation diagonals were measured under an optical microscope. Samples were sliced and metallographically polished prior to oxidation studies. Non-isothermal oxidation tests were carried out in a thermo gravimetric analyzer (TGA). The cyclic oxidation test was done for 15 cycles at 1300 °C. One cycle includes measuring the weight of the sample before oxidation, isothermal holding for 1 hour, kept for cooling to room temperature and measuring weight to record mass gain or loss. The constituent phases of the oxide scales were determined by XRD analysis. The structures of the oxide scales of the specimens were examined using a FESEM and EDX.

3. Results and Discussions

3.1 Densification

The effects of Y_2O_3 content on bulk and relative densities of the experimented samples are shown in Fig. 1. Figure 2 illustrates the influence of Y_2O_3 content on densification parameters and shrinkage of ZSBC composites. Results indicate that the relative density of the ZSBC-xY (x = 0/5/10/15 vol.% Y_2O_3) composites bears a direct proportionality with the volume fraction of Y_2O_3. Densification parameters of ZSBC-0Y composites have been found to vary from 0.76 ± 0.01 to 0.89 ± 0.04 when altering Y_2O_3 content from 0 to 15 vol.%. Figure 2 illustrates the variation of shrinkage with the volume fraction of Y_2O_3. It exhibits that the shrinkage increases with an increase in volume fraction of Y_2O_3 up to 10 vol.%, and then it decreases. Greater relative density has been obtained by a higher amount of Y_2O_3 that improves the densification behavior of the ZSBC-0Y composite.

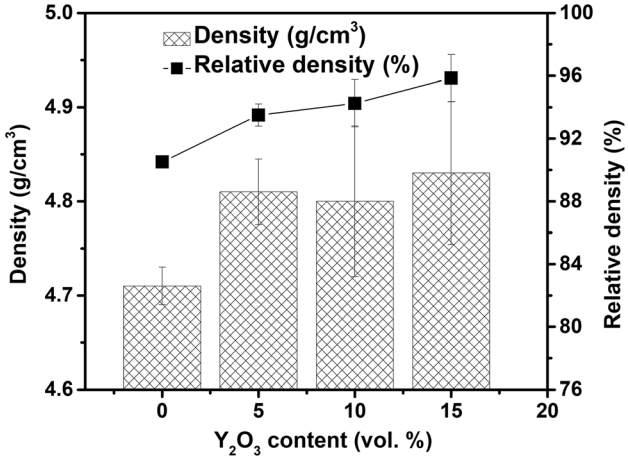

Fig. 1 Plot shows effect of Y_2O_3 content on density and relative density of ZSBC (0-15Y) composites compacted by 333 MPa pressure

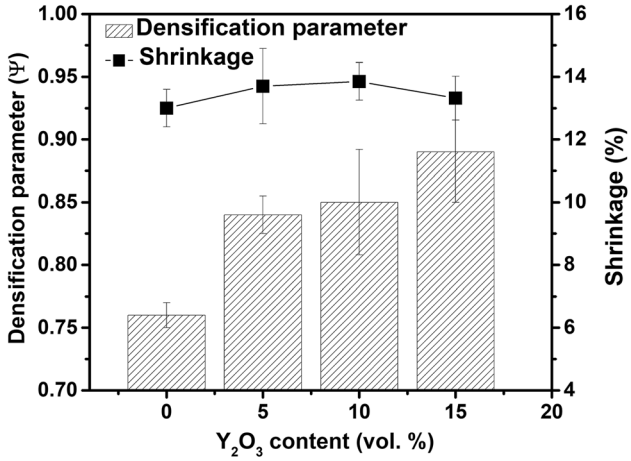

Fig. 2 Plot shows effect of Y_2O_3 content on densification parameter and shrinkage of ZSBC (0-15Y) composites

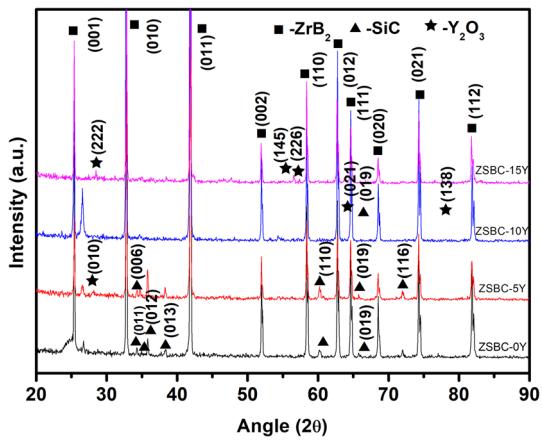

Fig. 3 Plot illustrates XRD patterns of pressureless sintered ZSBC (0-15Y) composites

XRD patterns of sintered ZSBC composites containing different Y_2O_3 content at 1750 °C are exhibited in Fig. 3. Peaks of ZrB_2 are the primary constituent phase along with SiC for the ZSBC composites. Peaks of Y_2O_3 are observed for the ZSBC composites containing Y_2O_3.

Secondary electron (SE) images of ZSBC-0Y, ZSBC-5Y, ZSBC-10Y, and ZSBC-15Y ceramic composite are presented in Fig. 4. The microstructure of the sintered samples exhibits uniformly distributed ZrB_2 and SiC phases. Figure 4 indicates that ZrB_2 appears bright, SiC looks grey, and B_4C shows dark. White Y_2O_3 particles are present at the junction point of three grains in the microstructures of ZSBC-5Y, ZSBC-10Y, and ZSBC-15Y composites. The average ZrB_2 grain sizes of ZSBC-0Y, ZSBC-5Y, ZSBC-10Y, and ZSBC-15Y composites are 11.05 ± 2.34, 10.25 ± 2.11, 9.22 ± 1.2, and 7.25 ± 2.6 μm, respectively.

Figures 5 and 6 depict microstructures and elemental mapping of different phases of ZSBC-0Y and ZSBC-15Y composites. EDX result (Fig. 6) indicates that Y_2O_3 particles are present at the triple junction of the grains. Y_2O_3 particles decrease average matrix grain size from 11.05 ± 2.34 to 7.25 ± 2.6 μm as Y_2O_3 content increases from 0-15 vol.%. Average grain size of ZrB_2 was calculated from SEM images. These images have been acquired from various locations of the composites. Results exhibit that the intermediate matrix (ZrB_2) grain size bears an inverse proportionality with the amount of Y_2O_3. The introduction of Y_2O_3 to ZSBC composite refines the grain sizes of ZrB_2, and subsequently, a more significant volume fraction of Y_2O_3 improves the densification properties of the developed composites.

3.2 Electrical Properties

The electrical behavior of the developed samples is displayed in Table 1. Incorporation of Y_2O_3 reduces the electric conduction of the ceramic materials. The electrical resistivity of Y_2O_3 (6.56×10^{-6} Ω-m) (Ref 55) is substantially higher than ZrB_2-20 vol. SiC (0.1×10^{-6} Ω-m) (Ref 23, 26). This, in turn, lowers the electric conduction of the ZSBC-Y (ZrB_2-SiC-Y_2O_3) ceramic material. Generally, the electric conduction of the composite materials reduces when an increasing number of interfaces are added (Ref 23, 26, 38). In the study of Mallik et al. (Ref 26), the electrical resistivity of ZrB_2 increases when SiC is added to the material. Adding 5 vol.% Y_2O_3 increases the electrical resistivity of the ZrB_2-20 vol.% SiC ceramic material by about 39.4%. Developing a more significant fraction of interfaces due to introducing Y_2O_3 (which possesses higher electrical resistivity) leads to decreased electrical conductivity. It is well established in the literature that factors like shape, dimensions, and different phase interfaces, apart from the volume percentage of the incorporated other phase, are the driving factors that govern the electrical properties of ceramic composites (Table 1).

Average electrical resistance of the internal interfaces was measured using Brick Layer Model (BLM) (Ref 56) for ZrB_2-SiC-Y_2O_3 composites considering the following relation:

$$\rho = [(1/\rho_{int}) + (R_I/d)]^{-1} \quad \text{(Eq 9)}$$

where ρ stands for electrical conductivity, ρint denotes the intrinsic electrical conductivity of the matrix phase, R_I implies the average electrical resistance of the internal interfaces, and δ is the average grain size of the matrix phase. In Eq 9, ρ_{int} of single crystal ZrB_2 matrix is taken ≈2.17×10^7 S/m (Ref 57). Eq 9 utilizes the EMA (effective medium approximation) to calculate γ. According to this technique, the secluded addition of more scattered phases is assumed to surround the matrix phase. The effective conduction in the matrix, the following equation is used to calculate the ρ_{eff} of every sample (Ref 58):

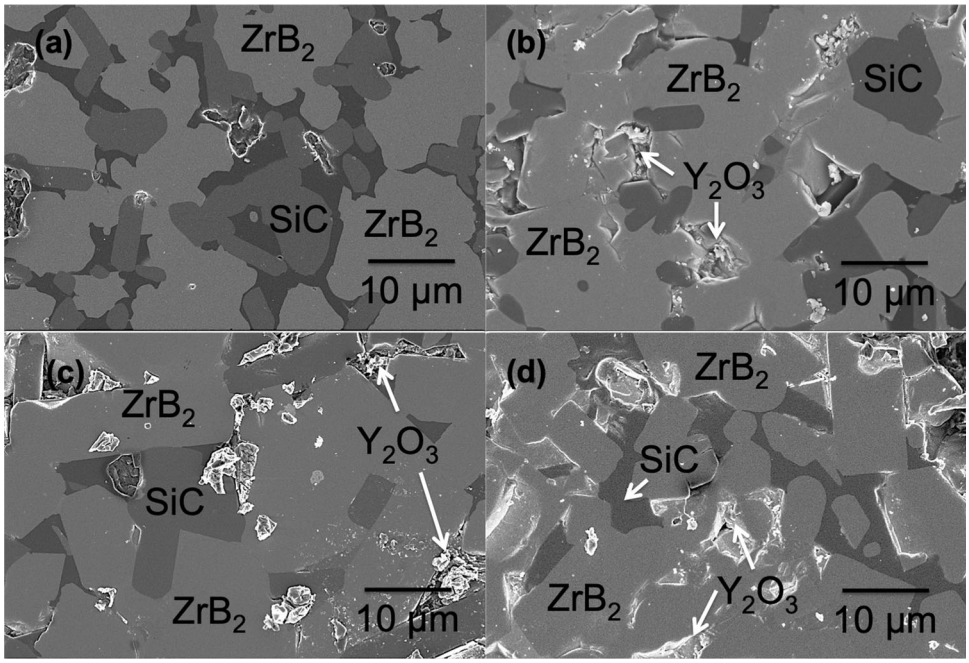

Fig. 4 Micrographs of (a) ZSBC-0Y, (b) ZSBC-5Y, (c) ZSBC-10Y and (d) ZSBC-15Y composites

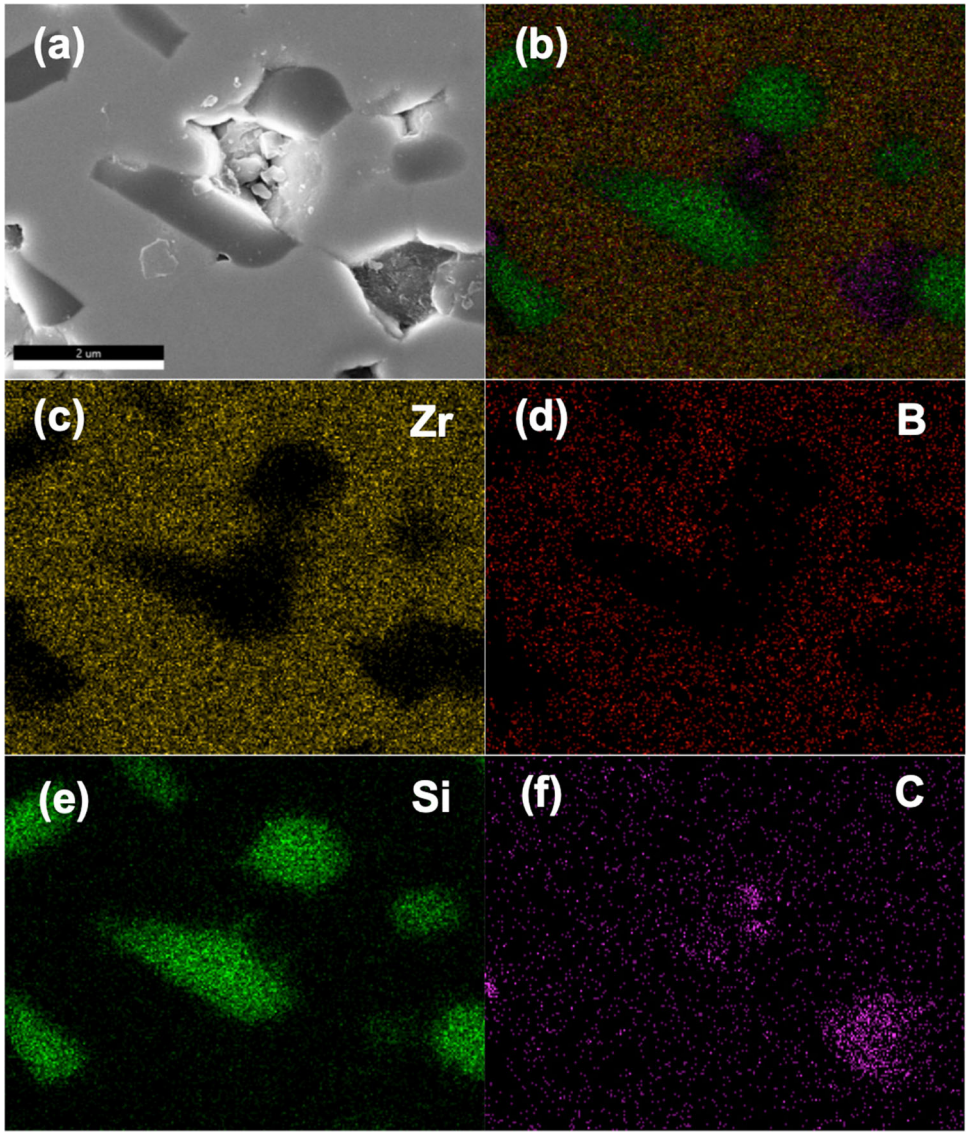

Fig. 5 Image depicting (a) FESEM image, elemental mapping analysis of (b) all, (c) Zr, (d) B, (e) Si, and (f) C of ZSBC-0Y ceramic composite

$$\sum_{i=1}^{N} \frac{\rho_{\text{eff}} - \rho_i}{2\rho_{\text{eff}} + \rho_i} f_i = 0 \qquad \text{(Eq 10)}$$

where electric conductivity for the i_{th} phase is denoted by ρ_i and f_i symbolizes the volume percentage for the i_{th} phase. The intrinsic electrical resistivity values of ZrB_2, SiC & Y_2O_3 are considered as 4.9 $\mu\Omega$-cm (Ref 59), 5×10^3 $\mu\Omega$-cm (Ref 60), and 650 $\mu\Omega$-cm (Ref 55) respectively. To calculate the ρ_I (= ρ_m) value for the matrix, ρ_{eff} in Eq 10 were replaced with the values for electrical conductivity obtained from experiments. The polycrystalline matrix phase resists the current flow from the grain boundaries, so the intrinsic conductivity varies from that of a single crystal material. Taking a value from Zhang et al. (Ref 57), in Eq 9, the value of ρ_{in} has been replaced by $\rho_{m.}$

R_I values computed for ZSBC-0Y, and ZSBC-5Y composites have been found 2.4×10^{-12} m^2-S^{-1}, and 2.86×10^{-12} m^2-S^{-1}, in order. The outcome shows R_I values change with the addition of Y_2O_3, which possesses higher electrical resistivity than ZrB_2. Further, the result illustrates that the ZSBC-0Y shows greater electrical resistivity of~3.7 times than the sintered material prepared by hot-pressing (Ref 23), while it is 1.3 times higher than pressureless sintered ZSBC-20 composites. However, the R_I value (2.4×10^{-12} m^2/S) of the ZSBC-0Y composite is more than ZrB_2-20vol.% SiC (1.5×10^{-13} m^2/S) (Ref 23). The higher porosity content in the pressure-less sintered ZSBC-0Y composite strongly influences the interfacial electrical resistivity by reducing it compared to the developed composites. Figure 7(a) represents the specific heats of ZSBC-xY (x = 0/5/10/15) composites with varying temperatures. The specific heat has been calculated by using ROM.

The thermal diffusivity of the ZSBC-xY composites is inversely proportionate with temperature because of a surge in phonon scattering, as shown in Fig. 7(b). The ZrB_2-SiC-based composite containing Y_2O_3 (ZSBC-15Y) shows lower thermal diffusivity at all temperatures than other investigated ZSBC-xY composites. Figure 7(c) shows the thermal conductivity values of ZSBC-xY composites with respect to temperature.

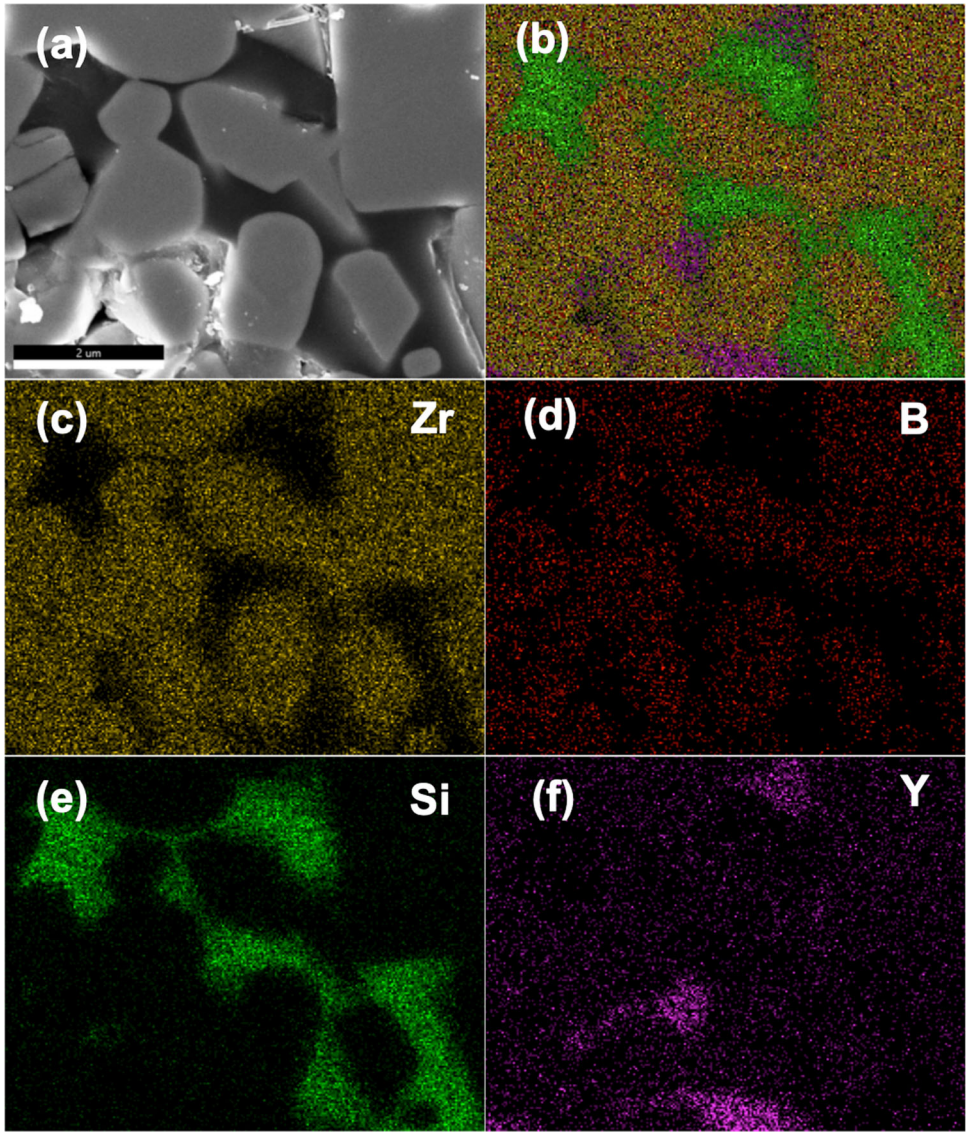

Fig. 6 Image depicting (a) FESEM image, elemental mapping analysis of (b) all, (c) Zr, (d) B, (e) Si, and (f) Y of ZSBC-15Y ceramic composite

Table 1 Electrical behavior of ZrB_2-SiC-Y_2O_3 ceramic materials at ambient temperature

Composites	Smple thickness, mm	Voltage, mV	Current, mA	Resistance, $\mu\Omega$	Resistivity, 10^{-8} Ω-m	Electrical conductivity, 10^6 S/m
ZSBC-0Y	1.9	0.0044	100	44	37.88	2.64
ZSBC-5Y	2.5	0.0046	100	46	52.11	1.92
ZSBC-10Y	2.5	0.005	100	50	56.64	1.77
ZSBC-15Y	2.5	0.0055	100	55	62.30	1.61

The thermal conductivity was calculated by Eq 6 using measured values of the thermal diffusivity, bulk density & heat capacity. The thermal conductivity value of ZSBC-15Y is lower than ZSBC-0Y in the experimented temperature range. The results show thermal conductivity at ambient temperature for ZSBC-0Y, ZSBC-5Y, ZSBC-10Y and ZSBC-15Y are 38.2 W/mK, 38.05 W/mK, 34.51 and 27.97, respectively, which are much lesser than reported values in previous studies about ZrB_2-SiC ceramics (Ref 23, 26). The Y_2O_3 addition greatly impacted thermal conduction by reducing thermal diffusivity.

At a particular temperature, the thermal diffusivity of ZSBC ceramic is governed by electron and phonon-based transport mechanisms (Ref 23, 57, 61). The influence of the electron component (λ_e) with respect to the thermal conductivity (λ) measured at ambient temperature is estimated utilizing the relation proposed by Zhang et al. (Ref 57).

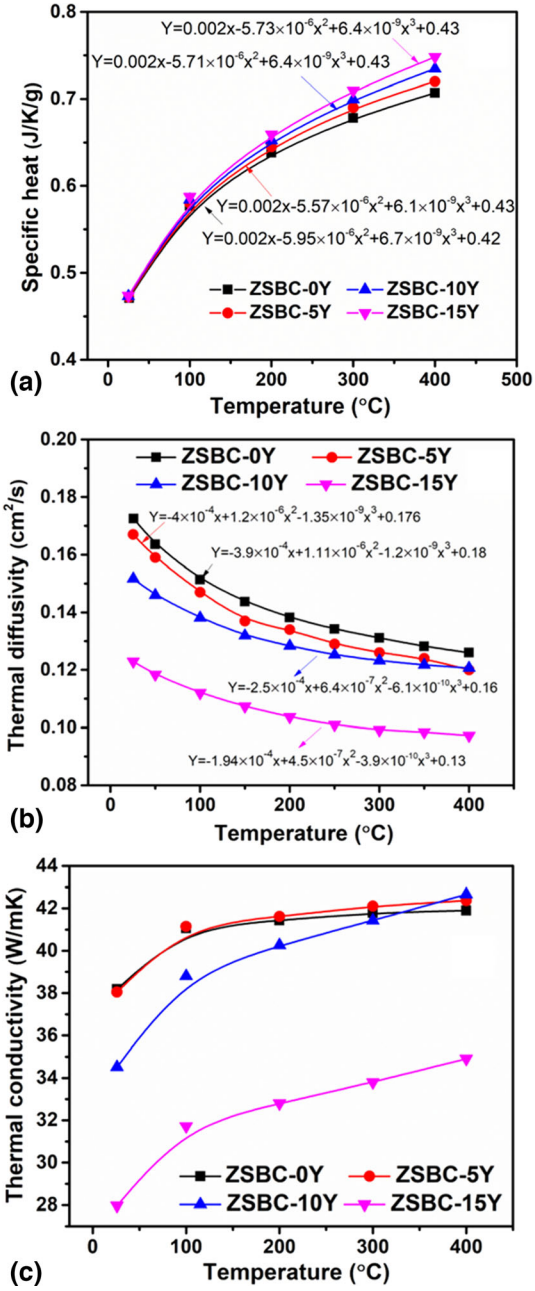

Fig. 7 Plots show the alteration of: (a) specific heat, (b) the thermal diffusivity and (c) thermal conductivity with temperature for ZSBC-0Y, ZSBC-5Y, ZSBC-10Y and ZSBC-15Y composites

$$\frac{\lambda_e}{\lambda} = 298\frac{L_0}{\rho \cdot \lambda} \quad \text{(Eq 11)}$$

where ρ and L_0 are the electrical resistivity and the Lorenz number (taken as 2.45×10^{-8} $W(\Omega K^2)^{-1}$) (Ref 57). The ratio of λ_e/λ for the ZSBC-0Y and ZSBC-5Y was calculated, and results indicate that the electronic contribution to thermal conductivity reduces with the addition of Y_2O_3. The calculated electronic contributions to thermal conductivity for ZSBC-0Y, ZSBC-5Y, ZSBC-10Y and ZSBC-15Y are 18.9, 14.03, 12.91, and 11.75 W/mK, respectively. This observation suggests that electrons facilitate thermal transport in the matrix phase (ZrB_2) and by phonons into the SiC and Y_2O_3 bonded covalently.

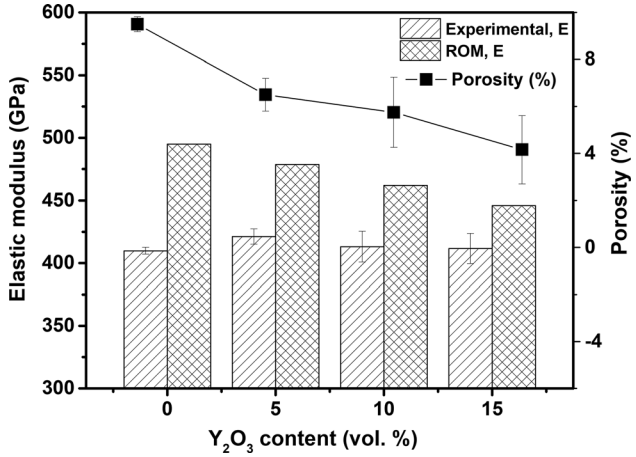

Fig. 8 Plot shows effect of Y_2O_3 content on elastic modulus of ZSBC (0-15Y) composites

3.3 Mechanical Properties

Figure 8 depicts experimentally obtained and calculated (ROM) Young's modulus and porosity content for ZSBC-xY composites with or without Y_2O_3. The rule of mixture (ROM) for Young's modulus (E_0) of a zero-porosity composite may be described as

$$E_0 = \sum_{i=1}^{n} E_i V_i \quad \text{(Eq 12)}$$

where n, E_i, and V_i are a total number of constituent phases, Young's modulus, and volume fraction, respectively of *i*th constituent phase. E_0 for investigated composites has been calculated considering theoretical Young's modulus of ZrB_2, SiC, and Y_2O_3 are 500 GPa,[5] 475 GPa,[68] and 171.5 GPa[69], respectively. The Young's modulus of the ZSBC-xY composites decreases with a higher amount of Y_2O_3 due to its lower Young's modulus value.

The Young's modulus values for the ZSBC-0Y (400 GPa) is close to ZSBC-20 (405 GPa) in our previous study. The experimentally attained Young's modulus is 9-17% lower than that of the corresponding ROM values. The presence of pores in the developed composites can be attributed to the deviations of Young's modulus and this deviation is minimum for the composites containing higher amount of Y_2O_3.

Effects of porosity and Y_2O_3 content on fracture toughness and hardness of ZSBC-Y composite material are revealed in Fig. 9. Result shows the mean value of hardness for the ZSBC-0Y, ZSBC-5Y, ZSBC-10Y, and ZSBC-15Y are 6.3 ± 0.33, 8.9 ± 0.6, 8.62 ± 0.3, and 9.6 ± 0.46 GPa, respectively. The hardness of the ZSBC-0Y composite is significantly lesser with respect to the reported values of the ZrB_2-20 vol.% SiC composite recorded in the study of Mallik et al. (Ref 35). The outcome recommends hardness strongly depends on densification as well as Y_2O_3 content.

Like the hardness, indentation fracture toughness is also influenced by Y_2O_3 content for investigated ZSBC composites. Figure 9 depicts that fracture toughness is proportionate with the amount of Y_2O_3 content. Indentation crack path interaction with particles describes the toughening mechanisms involved in the investigated composites. Figure 10 shows crack and particle interaction that leads to various phenomena such as crack

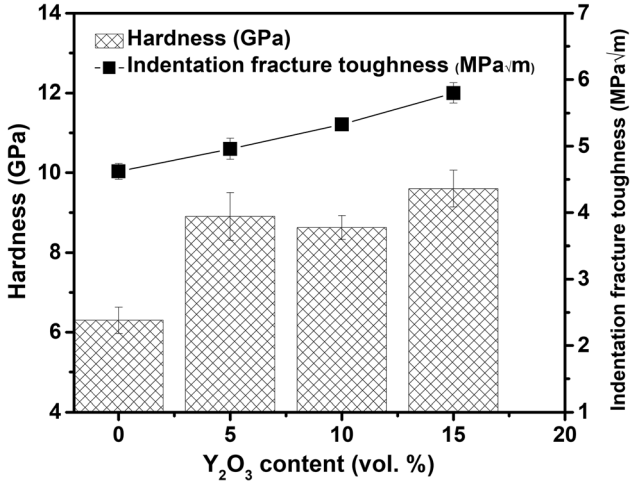

Fig. 9 Plot depicts variation of hardness and fracture toughness of ZSBC (0-15Y) composites with Y_2O_3 volume fraction

deflection, branching, and bridging. Such governing phenomena plausibly lead to the toughening of the sintered composites.

Fracture toughness is also proportionate with the volume percentage of Y_2O_3 content in the ZSBC ceramic. Figure 10(a) shows crack propagation in ZrB_2-SiC ceramic composite without Y_2O_3. Several researchers have found the fracture toughness of ZrB_2¬-20 vol.% SiC is maximum among the different variations with SiC content. In these figures, the crack gets deflected and follows a flexuous path that reduces the stress intensity. Figure 10(b) depicts the crack propagation in the ZrB_2-SiC with 5 vol.% of Y_2O_3. It is evident from these figures that the cracks cannot propagate as they deflected and interface debonding occurred. Becher et al. (Ref 64) suggested that interface debonding increases the crack opening displacement, improving the fracture toughness of ZSBC-Y ceramic material. Figure 10(c) shows how crack gets propagated in ZrB_2-SiC-10 vol.% Y_2O_3. The figures show that crack deflection and interface debonding reduce the stress intensity of the crack. Joining the broken particles with the crack surface lowers the stress intensity near the crack tip. Thus, it helps to arrest the crack. Moreover, the addition of Y_2O_3 reduces the sizes of the particles of the ZSBC-xY ceramic. Furthermore, it increases the fracture toughness value of the material.

3.4 Oxidation Behavior

Non-isothermal oxidation behaviors of ZSBC-0, ZSBC-5Y, ZSBC-10Y, and ZSBC-15Y composites are depicted in Fig. 11, and 12 shows XRD patterns of oxide scale formed during 2nd stage of oxidation. A separate non-isothermal oxidation has been carried out up to 1000 °C to understand the oxidation mechanism involved in this temperature regime. The expected reactions that took place during the oxidation test are as follows.

$$ZrB_2(s) + 5/2\ O_2(g) \rightarrow B_2O_3 + ZrO_2(s) \quad \text{(Eq 13)}$$

$$B_2O_3(l) \rightarrow B_2O_3(g) \quad \text{(Eq 14)}$$

$$4B_2O_3 + Y_2O_3(s) \rightarrow 2YBO_3 + B_2O_3 \quad \text{(Eq 15)}$$

$$2ZrO_2(s) + Y_2O_3(s) \rightarrow Zr_2Y_2O_7 \quad \text{(Eq 16)}$$

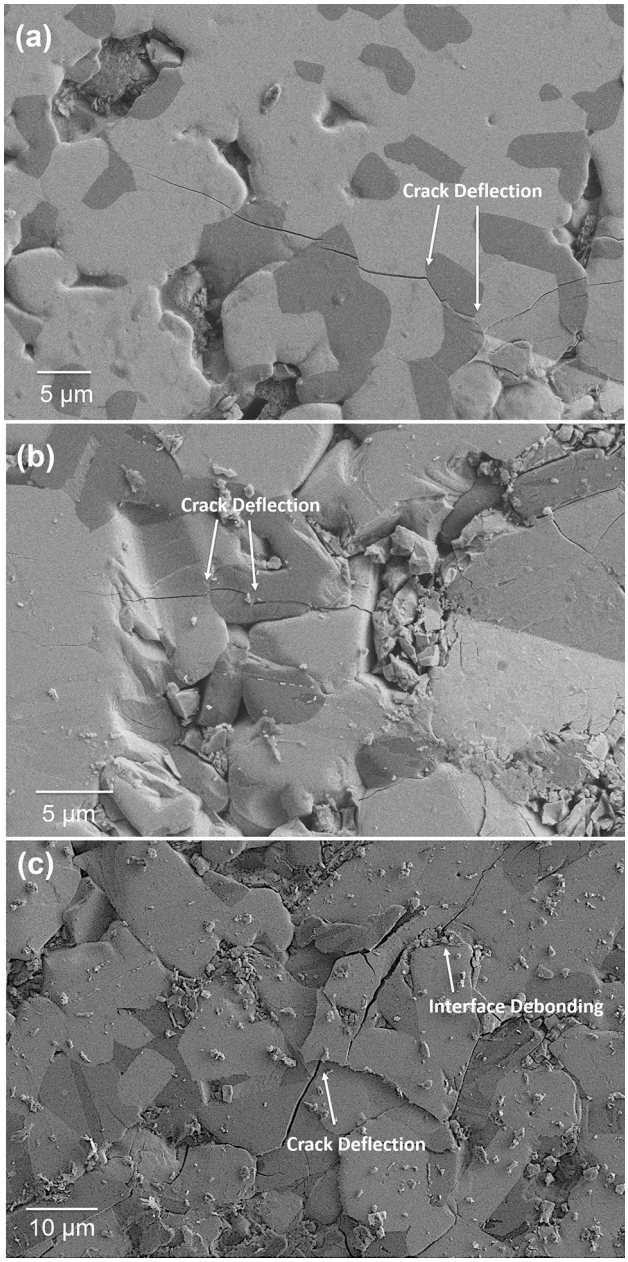

Fig. 10 SEM images indicate crack propagation in (a) ZSBC-0Y, (b) ZSBC-5Y and (c) ZSBC-15Y ceramic

$$SiC\ (s) + 3/2O_2(g) \rightarrow SiO_2(s) + CO\ (g) \quad \text{(Eq 17)}$$

$$SiO_2(s) + B_2O_3(l) \rightarrow SiO_2B_2O_3 \quad \text{(Eq 18)}$$

$$ZrO_2(s) + SiO_2(s) \rightarrow ZrSiO_4(s) \quad \text{(Eq 19)}$$

It is clear from the plots shown in Fig. 11 that the oxidation starts at approximately 740 °C by reaction (13) for ZSBC-0Y composite and increases at a constant rate up to 1100 °C. In this regime, monoclinic ZrO_2 (m- ZrO_2) and B_2O_3 (Fig. 12) are oxidation products. Due to the amorphous nature of B_2O_3, it is not identified in Fig. 12. As the temperature exceeded 1100 °C, oxidation of SiC was initiated by reaction (17), and further mass gain resulted. In contrast, oxidation begins at 740 °C by reaction (13) for ZSBC-5Y, ZSBC-10Y, and ZSBC-15Y

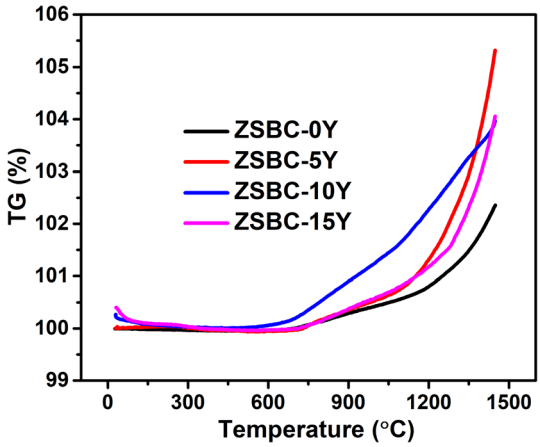

Fig. 11 Plots illustrating the change of mass versus temperature for ZrB_2-SiC-Y_2O_3 composites using different Y_2O_3 contents

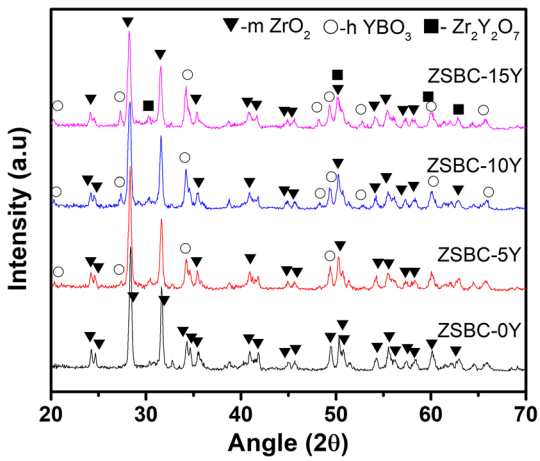

Fig. 12 X-Ray diffraction of oxide surfaces after non-isothermal oxidation up to 1000 °C of investigated composites

composites, and mass gain increases at a higher rate than ZSBC-0Y. Mass gain of the examined composites increases in ZSBC-0Y < ZSBC-5Y < ZSBC-15Y < ZSBC-10Y. During this temperature regime, B_2O_3 formed from reaction 12 reacted with Y_2O_3 and produced YBO_3 (reaction 15). The amount of YBO_3 increases in the order of ZSBC-5Y < ZSBC-10Y < ZSBC-15Y. The oxidation protection capability of B_2O_3 has been lost due to the formation of YBO_3, and as a result, more mass gain is observed for composites containing Y_2O_3. The utmost mass gain of ZSBC-10Y composite among all the investigated composites is attributed to the consumption of all Y_2O_3 to form YBO_3. However, the ZSBC-15Y composite contains more amount of Y_2O_3 that reacts with ZrO_2 according to reaction 16 and forms protective $Zr_2Y_2O_7$ (Fig. 12), and as a result, the composite regains its oxidation resistance. Lin et al. (Ref 65) also found that ZSY10 has higher mass gain than ZSY15 in thermogravimetric studies.

When the temperature exceeds 1200 °C, SiC oxidizes following reaction 17, and further mass gain is observed. Mass change after non-isothermal oxidation exposure for ZSBC-0Y, ZSBC-5Y, ZSBC-10Y and ZSBC-15Y composites are 2.4, 5.3, 3.97, and 4.1%, respectively.

Oxide scale characterization (Fig. 13 and 14) reveals that the oxide surface of ZSBC-5Y is comparatively rougher than that is

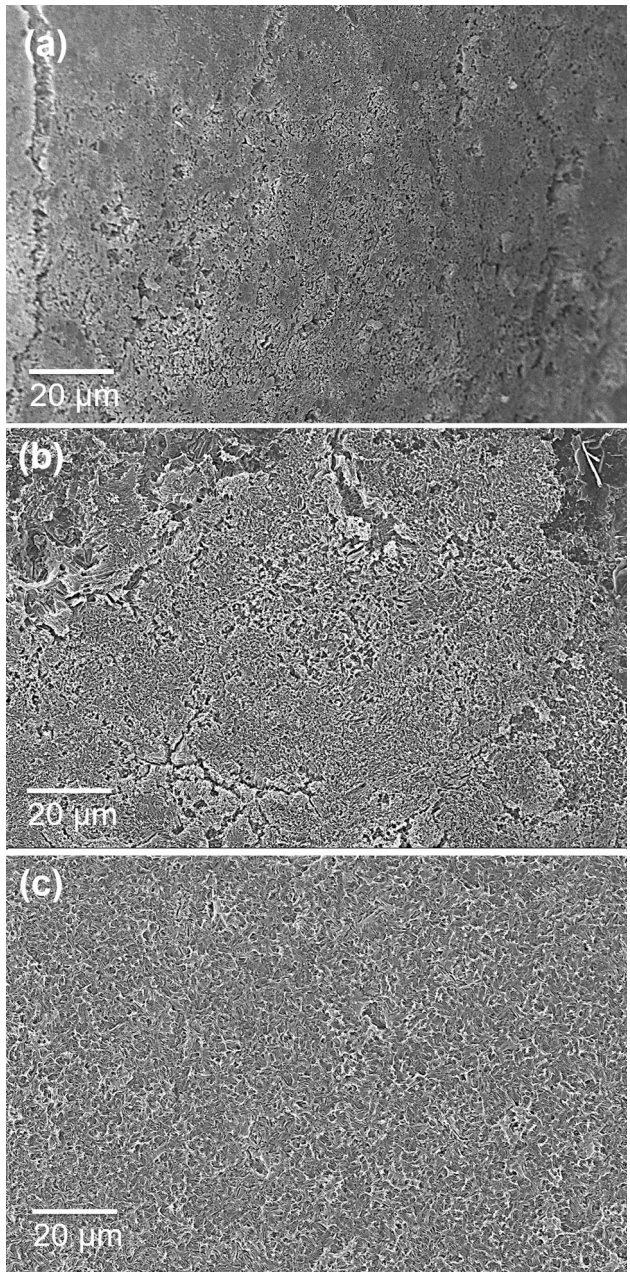

Fig. 13 FESEM microstructures shows that the oxide formed after non-isothermal oxidation test of (a) ZSBC-0Y, (b) ZSBC-5Y, and (c) ZSBC-15Y ceramic composites at low magnification

formed on the ZSBC-0Y, ZSBC-10Y and ZSBC-15Y composites. Pore formation at surfaces occurs due to the vaporization of B_2O_3 above ~ 1100 °C. Specimens (ZrB_2-SiC composite) after non-isothermal oxidation exposure show complete surrounded by borosilicate glassy layer with ZrO_2 precipitates which are agglomerated and form round shape (Fig. 13a and 14a). Round agglomeration shape turns into fibrous structures with the increase in Y_2O_3 content (Fig. 13b and c). This fibrous morphology formed due to the evolution of YBO_3 during oxidation. The subsurface layer becomes exposed due to this fibrous structure, through which oxygen can penetrate and oxidize the inner layer of the material. This fibrous formation rises with the volume content increment of Y_2O_3. It can be seen

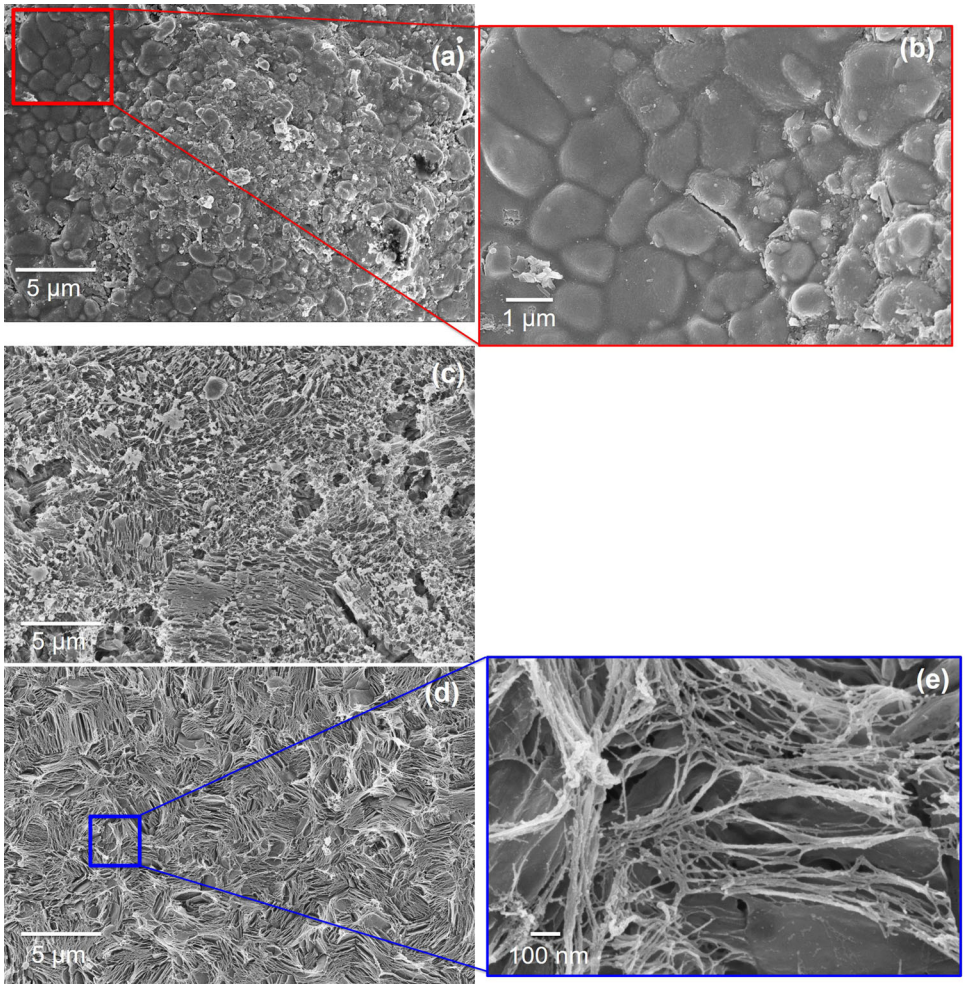

Fig. 14 FESEM microstructures shows that the oxide formed after non-isothermal oxidation test of (a-b) ZSBC-0Y, (c) ZSBC-5Y, and (d&e) ZSBC-15Y ceramic composites at high magnification

in Fig. 14(b) (c) and (d). The large gap between the fibers allows the oxygen atom to enter the sub-layers, which causes rapid material oxidation. As a result, the thickness of the oxide layer increased with the higher volume fraction of Y_2O_3 within the ZrB_2-SiC material. It leads to poor oxidation resistance of the material.

Figure 15(a), (b), and (c) depict plots of the kinetics of cyclic oxidation of ZSBC-xY composites at 1100, 1200, and 1300 °C for 12, 9, and 15 h, respectively. Figure 15(c) indicates that the ZSBC-0Y undergoes continuous mass gain up to the time span of 8 h. After that, stability can be seen due to insignificant mass change up to 12 h. The net mass-gain of the ZSBC-0Y composite is 20.46 mg/cm^2. The ZSBC-15Y shows the most mass change per area during the oxidation, followed by the ZSBC-5Y, indicating that the oxidation resistance property deteriorates by including Y_2O_3. Figure 16 depicts the XRD spectrum acquired from the oxide surfaces formed on the investigated specimens after cyclic oxidation at 1300 °C. Oxide scales mainly consist of monoclinic m-ZrO_2, $ZrSiO_4$, YBO_3 and SiO_2. The several oxides were produced through complete reactions (Reaction 13-15, 17, 19) of the investigated composites. XRD results also indicate the presence of YBO_3 in the oxidized ZSBC samples containing Y_2O_3. This compound formed at high-temperature oxidation of the samples made the fibrous and porous oxide layer. This type of surface is prone to oxidation, so incorporating Y_2O_3 deteriorated the oxidation resistivity of the ZrB_2-SiC-Y_2O_3 composites.

Figure 17 depicts the micrographs of oxide scales evolved during oxidation at 1300 °C. Characterization of oxidized samples through FESEM and EDX also confirms the formation of a thicker oxide layer over the samples containing Y_2O_3. Oxidation resistance property deteriorates with the inclusion of Y_2O_3. FESEM micrographs (Fig. 17) of oxide surfaces indicate the significant oxidation occur and thick oxide layer over the surface of the ZSBC-15Y specimen. Micrographs of ZSBC samples without Y_2O_3 show an oxide glassy layer with a high volume of silica. Oxidation at 1300 °C formed a few cracks on this glassy layer but much lesser than the cracks and pores formed over ZSBC-5Y, ZSBC-10Y and ZSBC-15Y. The addition of Y_2O_3 made the microstructure fibrous, and oxide atoms easily penetrate the outer layer and subsurface to oxidize the samples.

FESEM micrographs (Fig. 17) of ZSBC-5Y at three different temperatures show cracks on the surface, while it is more clearly visible in FESEM images of the oxidized samples at 1300 °C. Micrographs of ZSBC-10Y and ZSBC-15Y oxidized samples showed a thick but porous oxide layer, indicating the sample's poor oxidation resistance at 1300 °C.

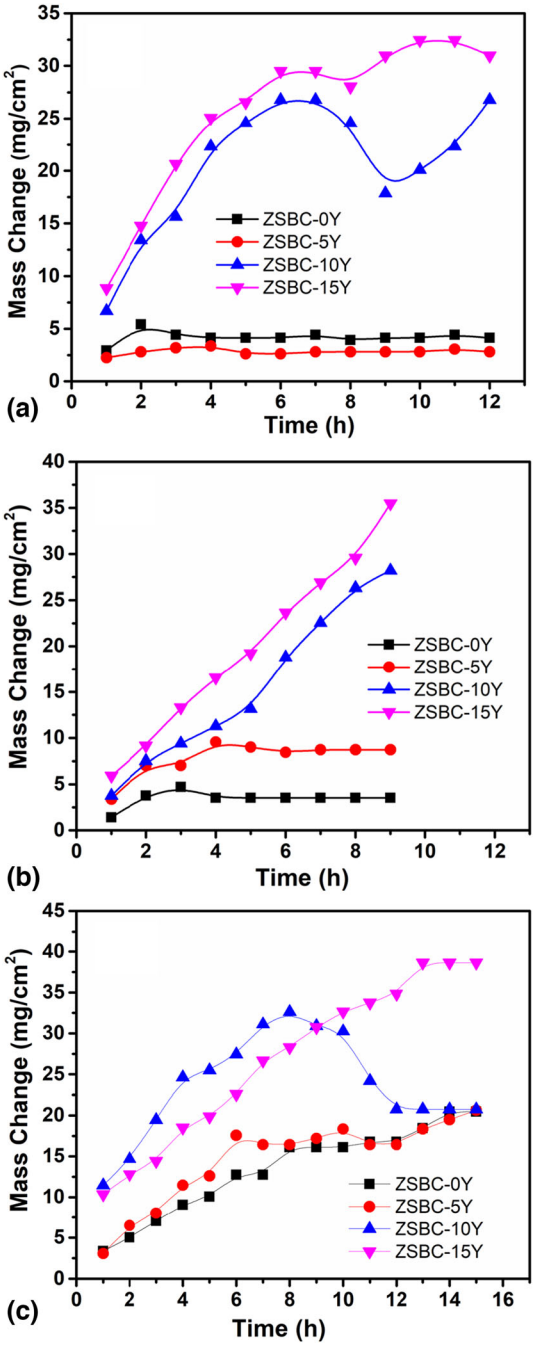

Fig. 15 Plots showing mass change in respect of time, during cyclic oxidation experiment at (a) 1100 °C, (b) 1200 °C and (c) 1300 °C

To understand the oxidation kinetics, the power law equation was applied which is

$$(\Delta W)^n = kt$$

where, n is measured for the materials oxidized at 1200 °C. The values of n and k (rate constant) are tabulated in Table 2.

The n value for the ZSBC-0Y material is the highest, which confirms the oxidation rate is slower than the other two samples. ZSBC-15Y showed the highest rate of oxidation among the samples, confirming the deterioration of the oxidation resistance property by adding Y_2O_3.

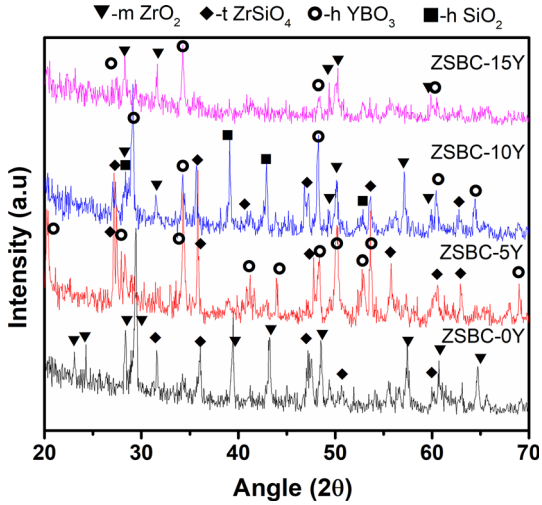

Fig. 16 X-Ray diffraction of oxide surfaces after cyclic oxidation at 1300 °C of investigated composites

Table 2 n value and rate constant (k) of materials oxidized at 1200 °C

Material	n	k
ZSBC-0Y	2.24	1.41
ZSBC-5Y	1.6	3.55
ZSBC-15Y	1.235	9.11

4. Conclusions

Pressure-less sintering has been successfully utilized to develop densified ZrB_2-SiC-Y_2O_3 composites with varying concentrations of Y_2O_3. The following are the significant findings of the current study:

(a) The presence of Y_2O_3 acts as an inhibitor for grain growth of the matrix phase, which has been observed from microstructural characterization.
(b) Physical properties like density and electrical resistivity of the ZrB_2-SiC-Y_2O_3 composites are observed to enhance as Y_2O_3 particles are introduced.
(c) Y_2O_3 addition diminished the thermal conductivities of the ZrB_2-SiC-Y_2O_3 composites.
(d) Mechanical properties like hardness and fracture toughness are observed to enhance with an increase in Y_2O_3 particle content
(e) The kinetics of cyclic oxidation at 1300 °C of ZSBC-15Y exhibits the maximum mass change per area during the oxidation followed by ZSBC-5Y, indicating that oxi-

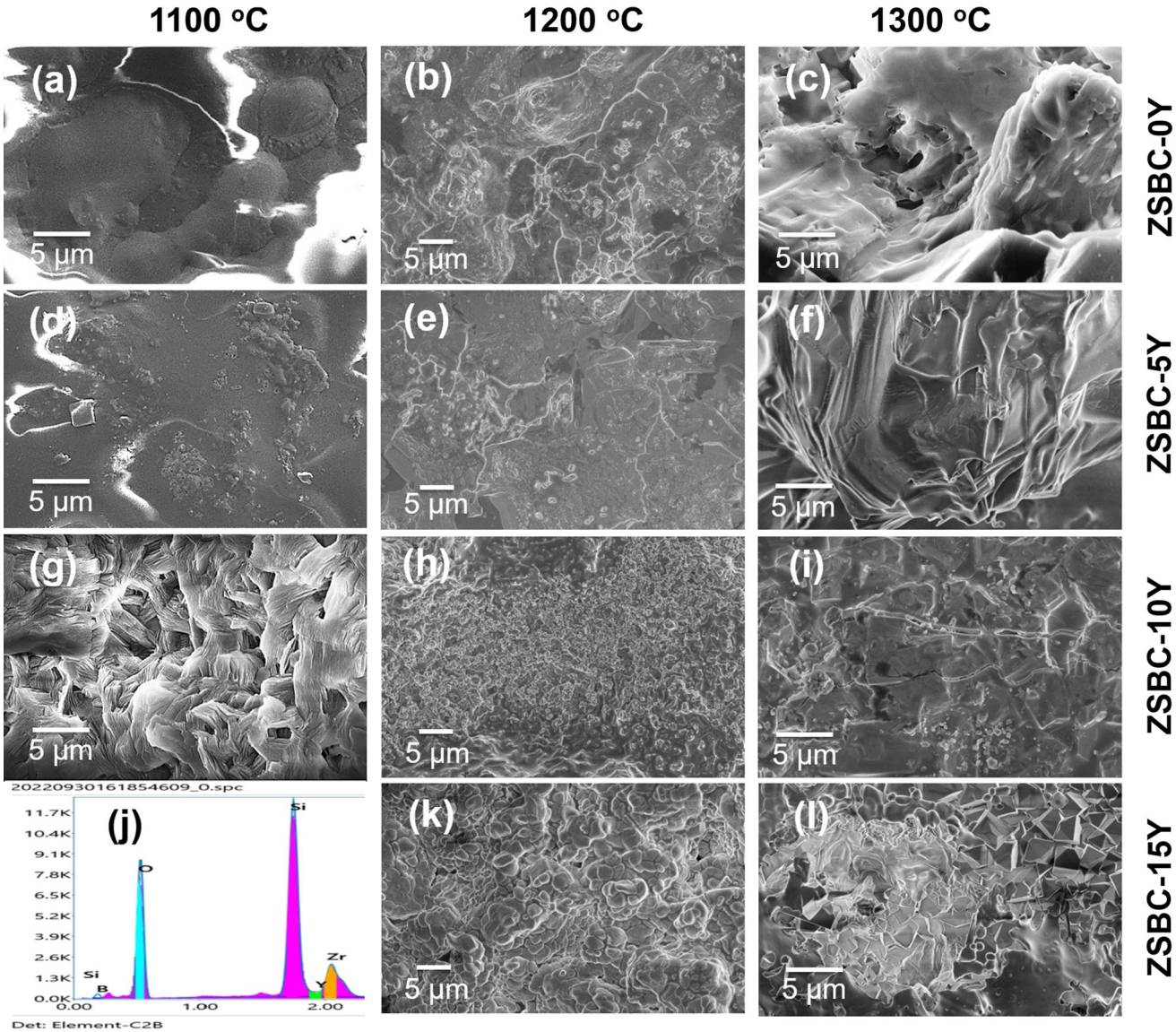

Fig. 17 Oxide scale formed after oxidation at different temperature of investigated ZSBC-xY composites (a-i, k, & l) and (j) EDX spectrum of figure (c)

dation resistance property deteriorates with the inclusion of Y_2O_3.

Acknowledgments

The project's financial support [DST, SERB, CRG/2019/004057] is gratefully acknowledged. The authors would like to express their appreciation to Dr. Lokesh C. Pathak, Chief Scientist, CSIR-National Metallurgical Laboratory, Jamshedpur, for permitting us to use their laboratory facilities. The authors acknowledge Dr. Gayatri Paul of Department of Production and Industrial Engineering, Birla Institute of Technology Mesra, Ranchi, Jharkhand, India for providing experimental facility for the thermal diffusivity measurement of the composites. The Field Emission Scanning Electron Microscope (Zeiss-SIGMA) facility at NIT Durgapur's Centre of Excellence in Advanced Materials has been recognized. The authors would also like to thank Mr. Shambhu Sarkar of COE NIT Durgapur for gathering FESEM and EDX data. We'd also like to thank Mr. Hiranmay Bairagya, of the XRD lab, for the XRD studies.

References

1. B.R. Golla, A. Mukhopadhyay, B. Basu, and S.K. Thimmapp, Review on Ultra-High Temperature Boride Ceramics, *Prog. Mater. Sci.. Mater. Sci.*, 2020, **111**, 100651. (**in English**)
2. A.L. Chamberlain and J.W. Zimmermann, Processing and Characterization of ZrB_2- Based Ultra-High Temperature Monolithic and Fibrous Monolithic Ceramics, *J. Mater. Sci.*, 2004, **39**(19), p 5951–5957. (**in English**)
3. E.W. Neuman, G.E. Hilmas, and W.G. Fahrenholtz, Processing, Microstructure, and Mechanical Properties of Large Grained Zirconium Diboride Ceramics, *Mater. Sci. Eng. A*, 2016, **670**, p 196–204. (**in English**)
4. M. Mallik, K.K. Ray, and R. Mitra, Oxidation Behavior of Hot Pressed ZrB_2-SiC and HfB_2-SiC Composites, *J. Eur. Ceram. Soc.*, 2011, **31**(1–2), p 199–215. (**in English**)

5. R.A. Cutler. Engineering properties of borides. Ceramics and Glasses, Engineered Materials Handbook, ASM International, Materials Park, OH, 1991, p.787–803
6. M.J. Gasch, D.T. Ellerby, and S.M. Johnson, Ultra High Temperature Ceramic Composites, *Handbook of Ceramic Composites*. N.P. Bansal Ed., Springer US, 2005, p 197–224. (**in English**)
7. K. Upadhya, J.M. Yang and W.P. Hoffmann, Materials for Ultrahigh Temperature Structural Applications, *Am. Ceram. Soc. Bull.*, 1997, **76**(12), p 51–56. (**in English**)
8. W.G. Fahrenholtz, G.E. Hilmas, I. Talmy, and J.A. Zaykoski, Refractory Diborides of Zirconium and Hafnium, *J. Am. Ceram. Soc.*, 2007, **90**(5), p 1347–1364. (**in English**)
9. S.R. Levine, E.J. Opila, M.C. Halbig, J.D. Kiser, M. Singh, and J.A. Salem, Evaluation of Ultra High Temperature Ceramics for Aero-propulsion Use, *J. Eur. Ceram. Soc.*, 2002, **22**, p 2757–3276. (**in English**)
10. M.M. Opeka, I.G. Talmy, E.J. Wuchina, J.A. Zaykoski, and S.J. Causey, Mechanical, Thermal, and Oxidation Properties of Refractory Hafnium and Zirconium Compounds, *J. Eur. Ceram. Soc.*, 1999, **19**(13–14), p 2405–2414. (**in English**)
11. A.K. Kuriakose and J.L. Margrave, The Oxidation Kinetics of Zirconium Diboride and Zirconium Carbide at High Temperatures, *J. Electrochem. Soc.Electrochem. Soc.*, 1964, **111**(7), p 827–831. (**in English**)
12 J.B. Berkowitz-Mattuck, High-Temperature Oxidation III. Zirconium and Hafnium Diboride, *J. Electrochem. Soc.Electrochem. Soc.*, 1966, **113**(9), p 908–994. (**in English**)
13. W.C. Tripp and H.C. Graham, Thermogravimetric Study of the Oxidation of ZrB_2 in the Temperature Range of 800–1500°C, *J. Electrochem. Soc.Electrochem. Soc.*, 1971, **118**(7), p 1195–1199. (**in English**)
14. D. Sciti, S. Guicciardi, A. Bellosi, and G. Pezzotti, Properties of a Pressureless-Sintered ZrB_2-$MoSi_2$ Ceramic Composite, *J. Am. Ceram. Soc.*, 2006, **89**(7), p 2320–2322. (**in English**)
15. Y. Yan, Z. Huang, S. Dong, and D. Jiang, Pressureless Sintering of High Density ZrB_2-SiC Ceramic Composites, *J. Am. Ceram. Soc.*, 2006, **89**(11), p 3589–3592. (**in English**)
16 S.C. Zhang, G.E. Hilmas, and W.G. Fahrenholtz, Pressureless Densification of Zirconium Diboride with Boron Carbide Additives, *J. Am. Ceram. Soc.*, 2006, **89**(5), p 1544–1550. (**in English**)
17. S. Zhu, W.G. Fahrenholtz, G.E. Hilmas, and S.C. Zhang, Pressureless Sintering of Zirconium Diboride Using Boron Carbide and Carbon Additions, *J. Am. Ceram. Soc.*, 2007, **90**(11), p 3660–3663. (**in English**)
18. W.G. Fahrenholtz, G.E. Hilmas, S.C. Zhang, and S. Zhu, Pressureless Sintering of Zirconium Diboride: Particle Size and Additive Effects, *J. Am. Ceram. Soc.*, 2008, **91**(5), p 1398–1404. (**in English**)
19 S. Zhu, W.G. Fahrenholtz, G.E. Hilmas, and S.C. Zhang, Pressureless Sintering of Carbon-Coated Zirconium Diboride Powders, *Mater. Sci. Eng. A*, 2007, **A459**(1–2), p 167–171. (**in English**)
20. A.L. Chamberlain, W.G. Fahrenholtz, and G.E. Hilmas, Pressureless Sintering of Zirconium Diboride, *J. Am. Ceram. Soc.*, 2006, **89**(2), p 450–456. (**in English**)
21. M. Mallik, S. Upender, R. Mitra, and K.K. Ray, Thermal Shock and Ablation Resistance of ZrB_2 Based Ultra-high Temperature Ceramic Composites. In: K.K. Kar, K. Muralidhar, J. Ramkumar editors. Proceeding in International Conference on Future Trends in Composite Materials and Processing INCCOM-6, Anamaya Publications, IIT Kanpur, 12-14 December 2007, p. 670-675, in English
22. T.R. Paul, M.K. Mondal, and M. Mallik, Thermal Shock Behavior of ZrB_2-$MoSi_2$-SiCw Composites, *J. Alloy. Compd.*, 2022, **924**, 166443. (**in English**)
23. M. Mallik, A.J. Kailath, K.K. Ray, and R. Mitra, Electrical and Thermophysical Properties of ZrB_2 and HfB_2 Based Composites, *J. Eur. Ceram. Soc.*, 2012, **32**(10), p 2545–2555. (**in English**)
24. S. Guo and Y. Kagawa, Thermal and Electric Properties in Hot-Pressed ZrB_2-$MoSi_2$-SiC Composites, *J. Am. Ceram. Soc.*, 2007, **90**(7), p 2255–2258. (**in English**)
25. G.V. Samsonov and I.M. Vinitskii, *Handbook of Refractory Compounds*, FI/PLENUM, New York, 1980. (**in English**)
26. M. Mallik, A.J. Kailath, K.K. Ray, and R. Mitra, Effect of SiC Content on Electrical, Thermal and Ablative Properties of Pressureless Sintered ZrB_2-Based Ultra-High Temperature Ceramic Composites, *J. Eur. Ceram. Soc.*, 2017, **37**(2), p 559–572. (**in English**)
27. M. Mallik, P. Mitra, N. Srivastava, A. Narain, S.G. Dastidar, A. Singh, and T.R. Paul, Abrasive Wear Performance of Zirconium Diboride Based Ceramic Composite, *Int. J. Refract. Metals Hard Mater.*, 2019, **79**, p 224–232. (**in English**)
28 T.R. Paul, M.K. Mondal, and M. Mallik, Dry Sliding Wear Response of ZrB_2-20vol.% $MoSi_2$ Composite, *Mater. Today Proc.*, 2018, **5**(2), p 7174–7183. (**in English**)
29. T.R. Paul, M.K. Mondal, and M. Mallik, Abrasive Wear Performance and Wear Map of ZrB_2-$MoSi_2$-SiC_w Composites, *J. Eur. Ceram. Soc.*, 2021, **41**(6), p 3227–3251. (**in English**)
30. D. Kalish, E.V. Clougherty, and K. Kreder, Strength, Fracture Mode, and Thermal Stress Resistance of HfB_2 and ZrB_2, *J. Am. Ceram. Soc.*, 1969, **52**(1), p 30–36. (**in English**)
31. S.Q. Guo, Densification of ZrB_2-Based Composites and their Mechanical and Physical Properties: A Review, *J. Am. Ceram. Soc.*, 2009, **29**(6), p 995–1011. (**in English**)
32. D. Sciti, F. Monteverde, S. Guicciardi, G. Pezzotti, and A. Bellosi, Microstructure and Mechanical Properties of ZrB_2-$MoSi_2$ Ceramic Composites Produced by Different Sintering Techniques, *Mater. Sci. Eng. A*, 2006, **434**(1–2), p 303–309. (**in English**)
33. W. Li, X. Zhang, C. Hong, W. Han, and J. Han, Microstructure and Mechanical Properties of Zirconia-Toughened ZrB_2-$MoSi_2$ Composites Prepared by Hot-Pressing, *Scr. Mater.*, 2009, **60**(2), p 100–103. (**in English**)
34. F. Monteverde, The Addition of SiC Particles into a $MoSi_2$-Doped ZrB_2 Matrix: Effects on Densification, Microstructure and Thermo-Physical Properties, *Mater. Chem. Phys.*, 2009, **113**(2–3), p 626–633. (**in English**)
35. M. Mallik, S. Roy, K.K. Ray, and R. Mitra, Effect of SiC Content, Additives and Process Parameters on Densification and Structure-Property Relations of Pressureless Sintered ZrB_2-SiC Composites, *Ceram. Int.*, 2013, **39**(3), p 2915–2932. (**in English**)
36. M. Mallik, R. Mitra, and K.K. Ray, Effect of Particulate Volume Fraction on Mechanical Properties of Pressure-Less Sintered ZrB_2-SiC Ultra-High Temperature Ceramic Composites, *Processing and Properties of Advanced Ceramics and Composites II: Ceram Trans: Wiley.* N.P. Bansal, J.P. Singh, J. Lamon, S.R. Choi, M.M. Mahmoud Ed., Hoboken, 2010, p 77–90. (**in English**)
37. S. Pan and H. Roy, Fracture Toughness Measurement of Hot Pressed ZrB_2-$MoSi_2$ Composite, *Int. J. Curr. Eng. Tech.*, 2013, **3**(5), p 1647–1652. (**in English**)
38. T.R. Paul, M.K. Mondal, and M. Mallik, Microstructure Dependent Physical and Mechanical Properties of Spark Plasma Sintered ZrB_2-$MoSi_2$-SiC_w Composites, *Int. J. Refract. Metals Hard Mater.*, 2019, **79**, p 131–137. (**in English**)
39. M. Mallik, K.K. Ray, and R. Mitra, Effect of Si_3N_4 Addition on Compressive Creep Behavior of Hot Pressed ZrB_2-SiC Composites, *J. Am. Ceram. Soc.*, 2014, **97**(9), p 2957–2964. (**in English**)
40 E. Ringdalen and M. Tangstad, Softening and Melting of SiO_2, an Important Parameter for Reactions with Quartz in Si Production, *Advances in Molten Slags, Fluxes, and Salts: Proceedings of the 10th International Conference on Molten Slags, Fluxes and Salts 2016*. R.G. Reddy, P. PinakinChaubal, C. Pistorius, U. Pal Ed., Springer International Publishing, Cham, 2016, p 43–51. (**in English**)
41 M. Mallik, K.K. Ray, and R. Mitra, Effect of Si_3N_4 Addition on Oxidation Resistance of ZrB_2-SiC Composites, *Coatings*, 2017, **7**(7), p 92. (**in English**)
42. M. Mallik, R. Mitra, K.K. Ray, Oxidation Behavior of Three ZrB_2 based Ultra High Temperature Ceramic Composites, in: Proceeding in SEICO 09 SAMPE EUROPE 30th International Jubilee Conference and Forum in March, Paris, 2009, pp. 467–474, in English
43 R. Mitra, M. Mallik, and S. Kashyap, High-Temperature Environmental Degradation Behavior of Ultrahigh-Temperature Ceramic Composites: Case Examples of Zirconium and Hafnium Diboride, *Handbook of Advanced Ceramics and Composites: Defense, Security, Aerospace and Energy Applications*. Y.R. Mahajan, R. Johnson Ed., Springer International Publishing, Cham, 2020, p 1221–1256. (**in English**)
44. A.L. Chamberlain, W.G. Fahrenholtz, G.E. Hilmas, and D.T. Ellerby, High Strength Zirconium Diboride-Based Ceramics, *J. Am. Ceram. Soc.*, 2004, **87**(6), p 1170–1172. (**in English**)
45. F. Monteverde, Beneficial Effects of an Ultra-Fine α–SiC Incorporation on the Sinterability and Mechanical Properties of ZrB_2, *Appl. Phys. A*, 2006, **82**(2), p 329–337. (**in English**)

46. D. Sciti, S. Guicciardi, A. Bellosi, and G. Pezzotti, Properties of a Pressureless Sintered ZrB_2-$MoSi_2$ Ceramic Composite, *J. Am. Ceram. Soc.*, 2006, **89**(7), p 2320–2322. (**in English**)
47 S.C. Zhang, G.E. Hilmas, and W.G. Fahrenholtz, Mechanical Properties of Sintered ZrB_2-SiC Ceramics, *J. Euro. Ceram. Soc.*, 2011, **31**(5), p 893–901. (**in English**)
48. J. Han, Hu. Ping, X. Zhang, S. Meng, and W. Han, Oxidation Resistant ZrB_2-SiC Composites at 2200**°**C, *Compos. Sci. Technol.*, 2008, **68**(3–4), p 799–806. (**in English**)
49. W.M. Guo and G.J. Zhang, Oxidation Resistance and Strength Retention of ZrB_2-SiC Ceramics, *J. Eur. Ceram. Soc.*, 2010, **30**(11), p 2387–2395. (**in English**)
50. X. Zhang, X. Li , J. Han, W. Han, and C. Hong, Effects of Y_2O_3 on Microstructure and Mechanical Properties of ZrB_2-SiC Ceramics, *J. Alloy. Compd.*, 2008, **465**(1–2), p 506–511. (**in English**)
51. C. Zhi-qiang, Z. Chang-ling, T. Ting-yan, S. Cheng-gong, S. Zhi-hong, and F. Jie, Pressureless Sintering of Ultra-high Temperature ZrB_2-SiC Ceramics, *Key Eng. Mater.*, 2008, **368**, p 1746–1749. (**in English**)
52. ASTME1461-01, Standard Test Method for Thermal Diffusivity of Solids by the Flash Method, 2008 (July21) http://www.astm.org/DATABASE.CART/ HISTORICAL/E1461-01.htm. in English
53. I. Barin, *Thermochemical Data of Pure Substance*, Wiley, Weinheim, 1989. (**in English**)
54. G.R. Anstis, P. Chantikul, B.R. Lawn, and D.B. Marshall, A Critical Evaluation of Indentation Techniques for Measuring Fracture Toughness: I, Direct Crack Measurements, *J. Am. Ceram. Soc.*, 1981, **64**, p 533–538. (**in English**)
55. B. Marappa, V. Pattar and M.S. Rudresha, Investigations of Structural, Optical and Electrical Properties of Cu^{2+} Doped Y_2O_3 Nanosheets, *Chem. Phys. Lett.Lett.*, 2019, **728**, p 57–61. (**in English**)
56. D.S. Smith, S. Fayette, S. Grandjean, and C. Martin, Thermal Resistance of Grain Boundaries in Alumina Ceramics and Refractories, *J. Am. Ceram. Soc.*, 2003, **86**(1), p 105–111. (**in English**)
57. L. Zhang, D.A. Pejakovic, J. Marschall, and M. Gasch, Thermal and Electrical Transport Properties of Spark Plasma- Sintered HfB_2 and ZrB_2 Ceramics, *J. Am. Ceram. Soc.*, 2011, **94**(8), p 2562–2570. (**in English**)
58. G. Grimvall Ed., *Thermophysical Properties of Materials*, 1st ed. Elsevier, North-Holland, 1999 (**in English**)
59. H. Kinoshita, S. Otani, S. Kamiyama, H. Amano, I. Akasaki, J. Suda, and H. Matsunami, Zirconium Diboride (0001) as an Electrically Conductive Lattice-Matched Substrate for Gallium Nitride, *Jpn. J. Appl. Phys.. J. Appl. Phys.*, 2001, **40**(12A), p L1280–L1282. (**in English**)
60. M. Nakabayashi, T. Fujimoto, M. Sawamura, N. Ohtani, (2010) Silicon Carbide Single Crystal, Silicon Carbide Single Crystal Wafer, and Method of Production of Same, U.S. Patent 7,794,842, in English
61. J.W. Zimmermann, G.E. Hilmas, W.G. Fahrenholtz, R.B. Dinwiddie, W.D. Porter, and H. Wang, Thermophysical Properties of ZrB_2 and ZrB_2-SiC Ceramics, *J. Am. Ceram. Soc.*, 2008, **91**(5), p 1405–1411. (**in English**)
62. C.K. Jun and P.T.B. Shaffer, Elastic Modulus of Dense Silicon Carbide, *Mater. Res. Bull.*, 1972, **7**(1), p 63–70.
63 W.R. Manning, O. Hunter Jr., and B.R. Powell Jr., Elastic Properties of Polycrystalline Yttrium Oxide, Dysprosium Oxide, Holmium Oxide, and Erbium Oxide: Room Temperature Measurements, *J. Am. Ceram. Soc.*, 1969, **52**(8), p 436–442. (**in English**)
64. P.F. Becher, C.H. Hsueh, P. Angelini, and T.N. Tiegs, Toughening Behavior in Whisker Reinforced Ceramic Matrix Composites, *J. Am. Ceram. Soc.*, 1988, **71**(12), p 1050–1061. (**in English**)
65. H. Lin, Y. Liu, W. Liang, Q. Miao, S. Zhou, J. Sun, Y. Qi, X. Gao, Y. Song ,and K. Ogawa, Effect of the Y_2O_3 Amount on the Oxidation Behavior of ZrB_2-SiC-Based Coatings for Carbon/Carbon Composites, *J. Eur. Ceram. Soc.*, 2022, **42**, p 4770–4782. (**in English**)